



Defective Bi@BiOBr/C microrods derived from Bi-MOF for efficient photocatalytic NO abatement: Directional regulation of interfacial charge transfer via carbon-loading

Ximing Li^a, Qibing Dong^a, Fei Li^{a,d,*}, Qiuwei Zhu^a, Qingyun Tian^a, Lin Tian^a, Yiyin Zhu^a, Bao Pan^b, Mohsen Padervand^{c,**}, Chuanyi Wang^{a,*}

^a School of Environmental Science and Engineering, Shaanxi University of Science and Technology, Xi'an 710021, PR China

^b School of Chemistry and Chemical Engineering, Shaanxi University of Science and Technology, Xi'an 710021, PR China

^c Department of Chemistry, Faculty of Science, University of Maragheh, P.O. Box 55181-83111, Maragheh, Iran

^d Key Laboratory for Advanced Materials, Centre for Computational Chemistry and Research Institute of Industrial Catalysis, School of Chemistry and Molecular Engineering, East China University of Science and Technology, Shanghai 200237, PR China



ARTICLE INFO

Keywords:

Electron-modulation engineering
Hierarchical Bi@BiOBr/C microrods
NO removal
Ohmic contact
Surface plasmon resonance

ABSTRACT

The implementation of precisely directional electron transfer at the interface of catalysts is still considered a huge challenge. Herein, hierarchical Bi@BiOBr/C microrods derived from a novel Bi-MOF were employed as a model to precisely construct the atomic-level interface electrons transfer channels via carbon-bismuth bonding. The optimized Bi@BiOBr/C with plasmonic Bi and oxygen vacancies exhibited a photocatalytic removal efficiency of 69.5 % for ppb-level atmospheric NO, which is 3.5 times higher than that of pure BiOBr (19.8 %). The enhanced photocatalytic performance is owing to precisely constructed electron transport channels with loaded graphitic carbon as a bridge (i.e., BiOBr → graphitic carbon → Bi nanoparticles). Further DFT calculations demonstrated the built-in graphitic carbon reconstructs an Ohmic contact with BiOBr and eliminates the Schottky barrier between BiOBr and Bi nanoparticles, enhancing the photoelectron transfer efficiency. This research represents an exciting case for the modulation of photoelectron transfer at the catalysts interface for air purification.

1. Introduction

Air pollution is one of the most serious challenges for human beings [1,2]. Nitric oxide (NO) is a common gaseous pollutant, which mainly originates from fossil fuels utilization and response to the formation of haze and photochemical smog [3,4]. Moreover, trace-level nitrogen oxides can cause damage to the lungs, heart, liver, and kidneys, seriously hazarding the respiratory system and leading to security issues for human health [5–7]. Therefore, the development of efficient and economical technologies to eliminate atmospheric NO has become a global concern [8]. Conventionally, some approaches have been employed to get rid of gaseous NO emissions, including selective catalytic reduction, thermal catalysis, biofiltration, and wet scrubbing [9–11]. However, these traditional methods are typically exploited for the elimination of high-concentration NO from industrial sources, which are not economical and appropriate for urban atmospheric conditions

with lower NO concentrations [12]. Thus, solar photocatalytic technology has been increasingly employed to effectively remove low-concentration of NO (~parts per billion (ppb)) because of its mild reaction conditions, low cost, and green easy-to-operate feature [13].

Semiconductor photocatalysis is regarded as an effective way to solve air pollution problems. As an advanced oxidation technology, it can purify ambient air pollutants by using the coupling of light and semiconductors to produce active species with redox capabilities [14, 15]. However, the majority of them behave with inferior light absorption properties, which restricts their application [16,17]. In this respect, as a ternary oxide with prominent physicochemical properties, BiOBr has an appropriate energy band, low toxicity, and favorable stability, showing a promising photocatalytic redox ability [18,19]. Its layered crystal structure is interleaved with $[Bi_2O_2]^{2+}$ slabs and dual-bromine atom layers, which makes it have a strong intrinsic polarization source and forms a spontaneous built-in electric field (IEF) for better charge

* Corresponding author at: School of Environmental Science and Engineering, Shaanxi University of Science and Technology, Xi'an 710021, PR China.

** Corresponding authors.

E-mail addresses: fayeli@sust.edu.cn (F. Li), padervand@maragheh.ac.ir (M. Padervand), wangchuanyi@sust.edu.cn (C. Wang).

separation [20,21]. BiOBr has attracted extensive research attention in the domains of solar-to-chemical energy conversion and air purification owing to its special photoelectric properties [22,23]. For instance, Liu and colleagues constructed BiOBr nanosheets by a facile hydrothermal process in the existence of CTAB and ethanol for the effective removal of gaseous benzene under UV light irradiation [24]. Li et al. fabricated $\text{Bi}_5\text{O}_7\text{Br}$ nanotubes by a low-temperature heat treatment procedure, which produced a large number of superoxide radicals and oxygen vacancies under visible light and achieved promising photocatalytic nitrogen fixation [25]. However, the disadvantages of poor adsorption capacity, low specific surface area, and slow kinetics still limit the actual development of BiOBr [26]. Therefore, to overcome these shortcomings, reasonable design and construction of efficient photocatalysts for practical air purification is of great significance.

Recently, porous crystalline metal-organic frameworks (MOFs) have been extensively employed as sacrificial templates for the construction of various nanomaterials due to the regular channels, ultra-high surface area, and adjustable structural functions [27–30]. For example, Zhu et al. reported that ZnO nanoparticles prepared from ZIF-8 with abundant oxygen vacancies (OVs) suggest selective NO-to- NO_3^- conversion [12]. Lu and co-workers prepared a ZIF-67-derived three-dimensional hollow mesoporous Co_3O_4 coated with two-dimensional g-C₃N₄ nanosheets and exhibited increased photocatalytic oxidation of NO [31]. In the meanwhile, the integration of plasma effects and defect engineering was proposed to promote the photocatalytic activity by hiking the light absorption and the charge separation efficiency of photocatalysts [32–34], and the cost-effective non-noble metal Bi exhibiting obvious plasma photocatalytic properties could be an alternative to the noble metal nanoparticles (Pt, Pd, Au) [35,36]. Therefore, Bi-based MOF derivatives incorporating dispersed Bi nanoparticles and defects on the surface have considerable potentials to be utilized in the field of photocatalytic air purification, which is barely investigated to date. In this regard, the reasonable synthesis and corresponding mechanism analysis of highly active Bi-based MOF derivatives are not only essential from a fundamental research perspective, they are also significant for the urban environmental NO abatement.

Herein, considering the advantages of MOFs as templates in the construction of nanomaterials, CAU-17 was employed as a precursor via a facile halogenation treatment and chemical reduction process to prepare a series of hierarchical microrods structured Bi@BiOBr/C

photocatalysts for effective NO conversion (Scheme 1). The optimized Bi@BiOBr/C microrods were implemented for photocatalytic abatement of ppb-level atmospheric NO with a photocatalytic efficiency of 69.5 % under visible light ($\lambda > 420$ nm). The precisely constructed electron transport channels with loaded graphitic carbon as a bridge enhance the directional migration of electrons and the separation of charge carriers. Among them, carbon atoms bonded to bismuth (Bi) and oxygen (O) atoms by electronic interaction were affirmed by XPS analysis, and an Ohmic contact constructed between BiOBr and the loaded graphitic carbon was verified by DFT calculations. Therefore, the photogenerated electrons from the conduction band (CB) edge of BiOBr could be directly injected into Bi nanoparticles along the BiOBr → graphitic carbon → Bi nanoparticles path, resulting in enhanced photocatalytic performance. Furthermore, the synergistic integration of a gradient concentration distribution of oxygen vacancies (OVs) and metallic Bi over Bi@BiOBr/C boosts visible light response and the generation of superoxide radicals as supported by the UV–Vis DRS and EPR analysis. The formation of toxic intermediate (NO_2) was effectively inhibited ($\text{C}_{\text{NO}_2} < 20$ ppb), owing to the increased production of reactive species ($\bullet\text{O}_2$) with an enhanced selectivity of NO-to- NO_3^- transformation, as proved by In-situ DRIFTS analysis.

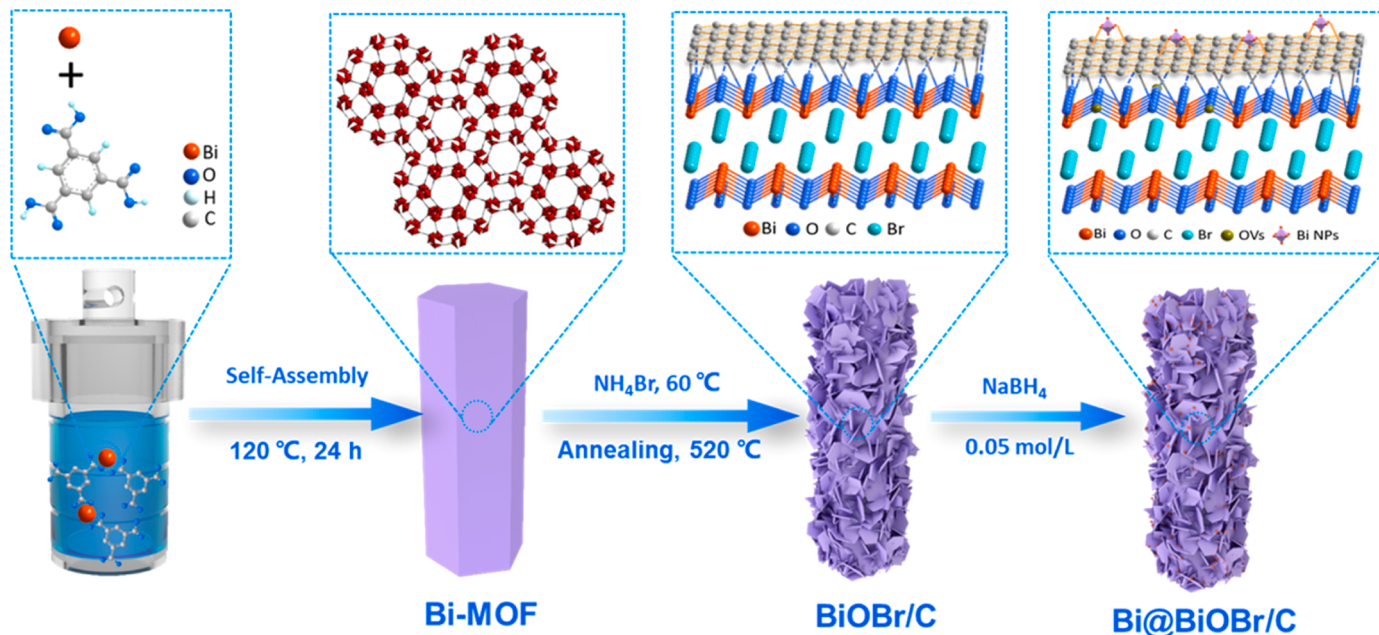
2. Experimental section

2.1. Chemicals and reagents

All of the chemical reagents that are available, involving bismuth nitrate pentahydrate ($\text{Bi}(\text{NO}_3)_3 \cdot 5\text{H}_2\text{O}$, 99 %), ammonium bromide (NH_4Br , 99 %), sodium borohydride (NaBH_4 , 99 %), 1,3,5-benzenetricarboxylic acid ($\text{C}_9\text{H}_6\text{O}_6$, 99 %), and methanol (CH_3OH , 99.5 %), were utilized without any additional purification.

2.2. Manufacture of Bi-based MOF (CAU-17)

The preparation of CAU-17 used the reported method with some modifications [37]. In a typical solvothermal preparation process, methanol (60 mL) solution of $\text{Bi}(\text{NO}_3)_3 \cdot 5\text{H}_2\text{O}$ (0.15 g, 0.3 mmol) and 1,3,5-benzenetricarboxylic acid (0.75 g, 3.5 mmol) was mixed, and after that, a 100 mL autoclave was filled with the resultant solution. The autoclave was preheated for 24 h at 120 °C. The resulting white powder



Scheme 1. Schematic representation of the fabrication process of Bi@BiOBr/C.

was produced by filtration, washed with methanol anhydrous three times, and then dried at 60 °C under vacuum overnight.

2.3. Manufacture of hierarchical BiOBr/C nanosheets

The hierarchical BiOBr/C nanosheets were obtained *in situ* by facile bromination of the CAU-17 using NH₄Br as the bromine source. Typically, 600 mg of the CAU-17 powders were dispersed in 60 mL of deionized water with constant stirring, and 0.012 mol of NH₄Br was added to the slurry within 20 min of agitating. After that, the ingredients were heated for 1 h at 90 °C in a water bath. After filtering and drying in a vacuum at 60 °C, the precipitates were heated at 520 °C for 3 h in a muffle oven with a temperature rise of 5 °C/min. After being cooled to room temperature naturally, the sample was harvested.

2.4. In situ synthesis of Bi@BiOBr/C

To introduce metallic Bi into BiOBr/C *in situ*, 0.1 g of BiOBr/C was first dispersed in 30 mL of deionized water, followed by the dropwise addition of aqueous NaBH₄ (0.05 mol/L) of a certain amount, and stirred for 2 h at room temperature. The precipitates produced were acquired by filtering, rinsed four times with ethanol and deionized water, and finally evaporated at 50 °C in a vacuum chamber. The as-obtained products containing NaBH₄ (0.05 mol/L) amounts of 1, 2, 3, and 4 mL were named Bi@BiOBr/C-1, Bi@BiOBr/C-2, Bi@BiOBr/C-3, and Bi@BiOBr/C-4, respectively.

2.5. Sample characterizations

On a Bruker D8 X-ray powder diffractometer implementing Cu K radiation ($\lambda = 0.1542 \text{ nm}$), the patterns of the photocatalysts as obtained were assessed using powder X-ray diffraction (PXRD). Both scanning and transmission electron microscopy (SEM, Hitachi Regulus8100, Japan; TEM, JEM-2100F, Japan) were used to examine the morphological structure of the photocatalysts while they were being created. The surface chemical properties of the catalysts were detected by X-ray photoelectron spectroscopy with Al K α X-ray radiation (XPS, AXIS Supra, UK). Implementing a scan UV-vis spectrophotometer (UV-3700, Shimadzu, Japan) and 100 % BaSO₄ as the reflection specimen, ultraviolet-visible diffuse-reflectance spectrometry (UV-vis DRS) was applied to examine the optical characteristics of the photocatalysts as-formed. The optical characteristics of the fresh specimens were assessed using photoluminescence spectroscopy (PL, LabRAM HR Evolution, Horiba, France). A Bruker E500 spectrometer was used to perform electron paramagnetic resonance (EPR) studies. Reactive oxygen species (ROSSs) were detected by employing the electron spin resonance (ESR) procedure using 5,5-dimethyl-1-pyrroline-N-oxide (DMPO). The photoelectrochemical properties of as-obtained photocatalysts were evaluated utilizing a three-electrode apparatus (CHI 660E, Chenhua, Shanghai). The working electrode was set up in the following manner before each test. A homogenous ink was created by dispersing 5.0 mg of the fresh catalysts in 0.02 mL of Nafion solution (5.0 wt %) with 0.98 mL of ethanol for 10 min. Following that, 10 μL of the slurry was pipetted onto a glassy carbon electrode that had already been manually polished and ultrasonically cleaned. A 300 W Xenon lamp (CEL-HXF300, Ceaulight, China) furnished with a UV cut-off filter (420 nm) served as the source of visible light irradiation.

2.6. The evaluation of visible-light photocatalytic activity

To investigate the photocatalytic activity of fresh catalysts, NO removal studies were conducted in a columnar continuously flowing device with a capacity of 0.785 L ($R = 5.0 \text{ cm}$, $L = 10 \text{ cm}$) at room temperature (Fig. S1). In this particular procedure, 50 mg of the specimen was dispersed in 10 mL of ethanol, and the mixture was then homogenized by 15 min of sonication before being put into a glass dish

with a diameter of 3.0 cm. Each specimen was then given a 60 °C pre-treatment to evaporate the ethanol before being set in the reactor's center. An ultraviolet filter (420 nm) was used to block out the ultraviolet light from a commercial 300 W Xenon lamp that was positioned vertically above the reactor. The airflow was accomplished by mixing the air and pure NO, which was regulated at 800 ppb and flowed at a rate of 12.9 $\text{mL} \cdot \text{min}^{-1}$ with the relative humidity of 5 % through the reaction container.

The photocatalytic assessment was carried out on a 42i (Thermo Scientific) NOx detector and was regularly collected every minute. The Xenon lamp was switched on when the as-prepared specimen attained the adsorption and desorption equilibrium. The abatement efficiency (η) of NO was computed as $\eta = (1 - C/C_0) \times 100 \%$, where C_0 and C are the feed and outlet port concentrations following the achievement of the adsorption-desorption equilibrium, respectively. Furthermore, the NO₂ generation concentration was measured and collected by a real time approach on the NOx detector. The purpose of the trapping experiments was to clarify the function of several active species during the photocatalytic reaction. Tert-butyl alcohol (TBA), potassium dichromate (K₂Cr₂O₇), p-benzoquinone (PBQ), and potassium iodide (KI) were implemented as the scavengers to catch hydroxyl radicals ($\bullet\text{OH}$), electrons (e^-), superoxide radicals ($\bullet\text{O}_2^-$), and holes (h^+), respectively. Typically, 50 mg of the catalyst was ultrasonically mixed with 2.0 mmol of the appropriate scavenger in 10 mL of ethanol. After that, the suspensions were put in glass dishes and the solvent was evaporated at 60 °C for usage afterward.

2.7. Research on photocatalytic NO abatement mechanism based on *in-situ* DRIFTS

To elucidate the reaction mechanism of the photocatalytic NO removal, the transient distribution of the intermediates and products during the adsorption and NO oxidation on the specimen surfaces was determined using *in-situ* DRIFTS. A TENSOR II FT-IR spectrometer (Bruker) was used to conduct *in-situ* DRIFTS evaluations of the photocatalysts in an intermittent flow setting (Fig. S2). The samples were pressurized and then put into the reaction chamber and heated for 20 min (120 °C) at a flow rate of 10 mL min^{-1} in a helium environment to remove the adsorbed contaminants on the surface of the specimen. When the temperature approached the intended point, the specimen was scanned into the infrared spectrum and used as a backdrop spectrum. Following that, 10 mL min^{-1} of NO and 10 mL min^{-1} of O₂ were delivered to the reaction vessel to saturate the NO adsorption on the photocatalysts. The catalyst was exposed to a 30 min sorption procedure in the dark while the adsorbed state of the specimen surface was examined. The specimen can achieve adsorption equilibrium after 30 min of dark adsorption. To assess the microscopic chemical reaction process of the reactant molecules on the catalyst surface, infrared spectra were acquired at various time intervals while the photoreaction procedure was conducted for 30 min with visible light illumination.

2.8. DFT calculations

All the DFT calculations were executed implementing the Vienna Ab initio Simulation Package (VASP) [38,39] with the core-valence electron interactions described by the projector-augmented wave (PAW) method [40,41] and the exchange-correlation effect presented by the Perdew-Burke-Ernzerhof (PBE) functional [42]. The C 2s2p, O 2s2p, Br 4s4p, and Bi 6s6p electrons were treated as valence electrons, as well as the spin-polarized effects of the electron considered during the calculations. Using plane-wave basis structures and an energy cutoff of 450 eV, the valence electronic states were enlarged.

The BiOBr was modeled as a redefined two-Bi₂O₂Br₂-layer BiOBr (001) slab (12.5 × 12.5 × 29 Å) based on the TEM results, and the layer C was modeled as a p (5 × 3) graphene (12.3 × 12.8 × 15 Å). The heterojunction (12.5 × 12.5 × 37 Å) was constructed by adding one

layer C on each side of BiOBr, with a small lattice mismatch of $<3\%$. The oxygen-deficient BiOBr was constructed by removing one oxygen atom from the BiOBr surface. The k-point mesh was employed as $1 \times 1 \times 1$, and the vacuum thickness between slabs was $\sim 15\text{ \AA}$. All the atoms except the bottom Br-Bi-O in the BiOBr slab and the bottom grapheme-Br-Bi-O in the heterojunction were permitted to relax until the atomic force threshold of $0.05\text{ eV}/\text{\AA}$. The electronic density of states (DOS) of independent BiOBr and C layer was leveled relative to the deep energy level of NO gas.

3. Results and discussion

3.1. Phase structure and element composition

The crystal structures and phase compositions of Bi-MOF, BiOBr/C, and Bi@BiOBr/C were analyzed by X-ray diffraction (XRD). The primary peaks and relative intensities in the XRD curves of the as-prepared Bi-MOF are consistent with those in the simulated curves (Fig. S3), proving

that a pure crystalline phase formed. The hierarchical BiOBr/C nanosheets were fabricated by a simple halogenation process of the precursor Bi-MOF, which served as the bismuth source and the framework of the hierarchical morphology. The chemical components of hierarchical BiOBr/C were verified by a well-matching XRD arrangement between the prepared specimen and the standard BiOBr (JCPDS No. 09-0393) and graphitic carbon (JCPDS No. 89-8497) curves (Fig. 1a). The peaks at $2\theta = 10.90^\circ, 21.92^\circ, 25.15^\circ, 31.69^\circ, 32.22^\circ, 46.20^\circ$, and 57.11° are allocated to the (001), (002), (101), (102), (110), (200), and (212) crystal planes of BiOBr, respectively. The broad diffraction peak with a center angle of 26.5° is equivalent to the (002) plane of graphic carbon. Then, since the deposition of metallic Bi on BiOBr/C could facilitate the crucial photocatalysis steps in the separation and transfer of charges, we adopted NaBH₄ as a reducing agent to obtain Bi-metal deposition from lattice Bi ions in BiOBr/C. The peaks at $2\theta = 27.16^\circ$ and 37.94° are assigned to the (012) and (104) crystal planes of metallic Bi (JCPDS No. 44-1246), respectively (Fig. 1b). The XRD patterns of Bi@BiOBr-C-X ($X = 1, 2, 3, 4$) showed that the diffraction peaks of Bi-metal appear

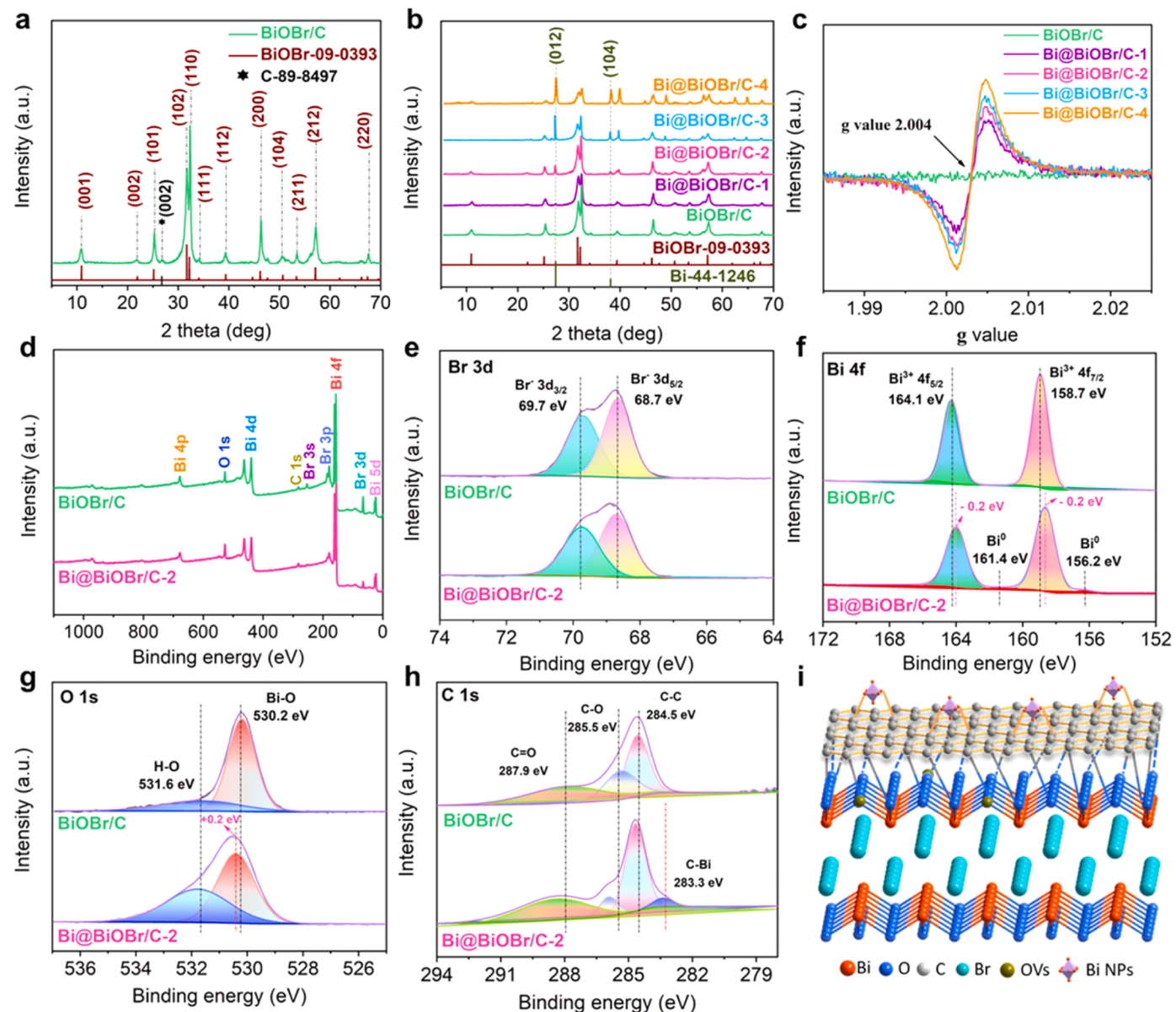


Fig. 1. The phase architecture and elemental composition of the fresh samples. XRD spectra of BiOBr/C (a) and Bi@BiOBr/C (b), EPR spectrum of BiOBr/C and Bi@BiOBr/C specimens (c), XPS spectrum of BiOBr/C and Bi@BiOBr/C-2: full scan (d), Br 3d (e), Bi 4f (f), O 1s (g), and C 1s (h), a schematic structure diagram of Bi@BiOBr/C (i).

and their intensities gradually heighten with the increased amount of added NaBH₄, while those of BiOBr/C become weaker. These results demonstrated that the dispersion of metallic Bi on the BiOBr/C substrate produces a shielding effect, leading to an attenuation of BiOBr/C XRD patterns [43].

Oxygen vacancies (OVs) in the lattice structure often serve as the electron traps, which renders them as paramagnetic centers to be detected by electron paramagnetic resonance (EPR) [44,45]. The presence of OVs in the BiOBr/C system was hardly observed since the EPR signal at $g = 2.004$ was negligible (Fig. 1c), while those in the Bi@BiOBr/C specimens were detected intensively and the EPR signals were gradually boosted as the loaded Bi-metal increased, suggesting the production of OVs in BiOBr could be triggered by the reduction of Bi ions from BiOBr, consistent with previous reports[33]. OVs can provoke the generation of intermediate energy levels, permitting photo-electrons to be aroused from the valence band (VB) to the mid-gap level and finally to the CB, thereby inducing subsequent photoreaction. Additionally, OVs can also serve as active centers, which play a pivotal role in the electronic reconfiguration of the Bi@BiOBr/C system, contributing to the provision of active sites for the adsorption/activation of small molecules (e.g., NO, O₂, and H₂O) and enhancing the formation of reactive species ($\cdot\text{O}_2$). Therefore, the coexistence of metallic Bi and OVs in Bi@BiOBr/C is confirmed by XRD diffraction peaks and EPR signals. Such co-modification of Bi-metal and OVs regulates the electronic structure of Bi@BiOBr/C and boosts the adsorption of NO and O₂ on active sites, which can promote the chemical activation of the reactants. In detail, according to Lewis's acid-base theory, OVs can facilitate surface electron reconfiguration, which is favorable to furnish active sites for NO adsorption. Bi-metal with SPR effects and functioning as electron sinks improves the light response and charge separation efficiencies. These are the influencing factors for photocatalytic performance enhancement.

The geometric and electronic structures of BiOBr/C and Bi@BiOBr/C specimens were further inspected by X-ray photoelectron spectroscopy (XPS) measurements. As shown in Fig. 1d, the peaks of the Bi 4f, Br 3d, O 1s, and C 1s states are apparent for both BiOBr/C and Bi@BiOBr/C-2. Specifically, relevant high-resolution spectrums showed that the peaks of Br 3d_{3/2} and Br 3d_{5/2} were situated at 69.7 and 68.7 eV, assigned to Br⁻ in BiOBr/C and Bi@BiOBr/C-2 (Fig. 1e). From the spectrum of Bi 4f in Fig. 1f, it can be seen that the two dominant peaks at 164.1 and 158.7 eV of the BiOBr/C sample belong to the Bi 4 f_{5/2} and Bi 4 f_{7/2} peaks of Bi³⁺, respectively. In regard to Bi 4f, the two extra peaks at 161.4 and 156.2 eV in Bi@BiOBr/C-2 compared with BiOBr/C further demonstrated the existence of reduction product Bi⁰, along with the slightly downshifted peaks of Bi³⁺ 4 f_{7/2} and Bi³⁺ 4f_{5/2} owing to the increased shielding effect of the higher electron cloud density of the metal ions. The O 1s peaks at 530.2 and 531.6 eV correspond to the O atoms in the BiOBr/C (Bi-O) crystal lattice and hydrated species O-H, respectively (Fig. 1g). The occurrence of OVs in Bi@BiOBr/C-2 introduces excess electrons to the system, resulting in the peak of Bi-O upshifting relative to that of BiOBr/C (530.2 eV), consistent with previous studies [43]. In addition, the binding energies of Bi 4f and O 1s peaks of Bi@BiOBr/C-2 were shifted to lower and higher by 0.2 eV, respectively, compared to BiOBr/C, indicating the existence of electronic interactions between Bi-metal and BiOBr/C. As illustrated in Fig. 1h, besides the C-C, C-O, and C=O bonds (the peaks at 284.5, 285.5, and 287.9 eV, respectively), the extra C-Bi bonds (the peak at 283.3 eV) appear in the Bi@BiOBr/C-2 graph whereas do not exist in the BiOBr/C graph, reflecting the critical role of carbon atoms as bridges to connect metallic Bi and BiOBr with Bi-C-O bonds, as depicted in Fig. 1i. These specific Bi-C-O bonds may promote the interfacial photo-carriers transfer efficiently, elevating the photocatalytic performance of as-designed materials.

3.2. Texture and morphology characteristics

The morphologies and structures of Bi-MOF, BiOBr/C, and

Bi@BiOBr/C-2 were assessed by scanning electron microscopy (SEM) and transmission electron microscopy (TEM). As one can see in Fig. 2a and b, the SEM images of synthesized Bi-MOF exhibit smooth rod-like morphology with a length of approximately 2.5 μm and about 200 nm in diameter. Derived from that, the synthesized BiOBr/C and Bi@BiOBr/C-2 still retain the rod shape but form rough hierarchical structures assembled by a large number of nanosheets (Fig. 2c and d). To further analyze the composition and architecture of the prepared specimens, their high-resolution TEM (HRTEM) images were taken and shown in Fig. 2e-g. Notably, the fringes of BiOBr(001), Bi(012), and C(002) crystal planes (corresponding to the spacings of 0.81, 0.32, 0.36 nm, severally) were observed clearly, suggesting the successful preparation of BiOBr/C and Bi@BiOBr/C-2 (also proved by the selected area electron diffraction (SAED) in Fig. 2h). Meanwhile, the significant diffraction rings in SAED graphics are in good agreement with the (012) plane of Bi-metal, (002) plane of graphitic carbon, and (001) and (012) planes of BiOBr in Bi@BiOBr/C-2. In addition, the in situ generated Bi nanoparticles with an average particle size of 4.0 nm were distributed on the substrate of BiOBr/C nanosheets (Fig. 2f and g, HRTEM), which conventionally exhibits SPR effect beneficial to the visible light adsorption capture and the charge separation of photocatalysts [32,33]. Furthermore, High-angle annular dark-field scanning transmission electron microscopy (HAADF-STEM) and energy-dispersive X-ray spectroscopy (EDS) analysis and elemental mapping images (Fig. 2i) also demonstrated that Bi, O, Br, and C elements were evenly distributed over the entire Bi@BiOBr/C-2. Among them, the mass fraction of each atom is C (5.59 wt %), O (10.39 wt %), Br (19.82 wt %), and Bi (64.20 wt %), respectively (Fig. S4). Based on the XPS and EDS measurements, the mass fraction is further derived for Bi⁰ (0.96 wt %), and BiOBr(93.45 wt %) in the Bi@BiOBr/C-2 system (Table S1). These analyses comprehensively introduce the texture and morphology characteristics of the acquired specimens.

3.3. Photocatalytic NO conversion

To assess the performance of the as-obtained photocatalysts, ppb-NO abatement examination was performed with the irradiation of visible light ($\lambda \geq 420$ nm) in a continuous air flow glass reactor. As shown in Fig. 3(a-b), the activity of the original Bi-MOF was negligible, and its NO removal rate was only around 0.6 %. After calcination, the Bi-MOF-derived layered BiOBr/C showed a better photocatalytic activity with a removal rate of 46.3 % compared to pure BiOBr (19.8 %) prepared by conventional methods (Fig. S5). However, the photocatalytic NO removal behavior of Bi@BiOBr/C-x photocatalysts exhibits a Gaussian distribution trend [46], that is, with the increase of Bi amount, the reactivity of Bi@BiOBr-x samples first boosts and then decreases (Fig. 3b). The reason is that the Bi-metal content exceeding the optimal value would lead to a negative impact instead since the excess Bi-metal can function as the recombination sites of photogenerated electrons and holes, making the photocatalytic NO oxidative activity decrease [43, 47]. Among them, Bi@BiOBr/C-2 exhibited the highest NO abatement efficiency of 69.5 %. Notably, the photocatalytic reactivity of Bi@BiOBr/C-2 was superior to most of the reported photocatalysts (Fig. S6). In addition, given that the stability of photocatalysts is vital for industrial applications, four consecutive catalytic oxidation experiments were performed with the Bi@BiOBr/C-2 catalyst. The removal efficiency is only slightly reduced by 6.5 % after four recycling cycles, revealing that it owns favorable stability (Fig. 3c). Moreover, NO₂, an intermediate produced during the photo-oxidation process, is usually more toxic than NO. Therefore, it is important to reduce NO₂ production during NO photo-oxidation. Intriguingly, as shown in Fig. 3d, the formation of the toxic intermediate (NO₂) of Bi@BiOBr/C-2 is effectively inhibited ($\text{C}_{\text{NO}_2} < 20$ ppb), much lower than the NO₂ generation concentration of 87 ppb for BiOBr/C. The enhanced photocatalytic performance is owing to precisely constructed electron transport channels with loaded graphitic carbon as a bridge, which facilitates the directional transfer of

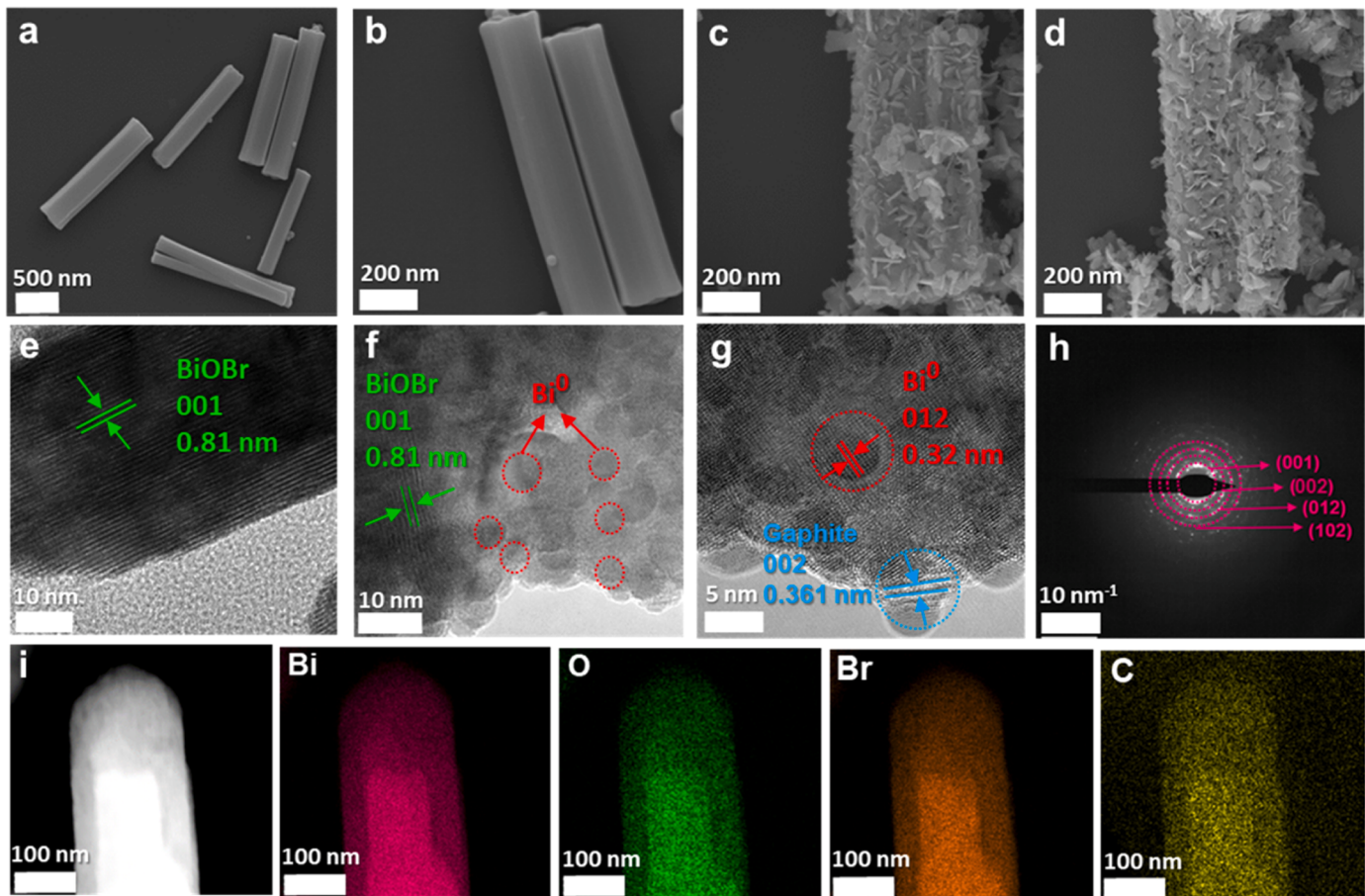


Fig. 2. SEM of Bi-MOF (a)-(b), BiOBr/C (c) and Bi@BiOBr/C (d), TEM of BiOBr/C (e), Bi@BiOBr/C-2 (f)-(g), SAED of Bi@BiOBr/C-2 (h) and HAADF elemental mapping of Bi@BiOBr/C-2 (i).

electrons and the separation efficiency of charges, as discussed in the following sections. Furthermore, the DeNOx index is applied to assess the relative toxicity of air containing NO and NO₂ and it was calculated from Eq. S1. As shown in Fig. 3e, BiOBr/C had the highest NO₂ production and the lowest DeNOx index (+0.22), so it was not considered to be an environmentally friendly photocatalyst. The co-modification of Bi-metal and OVs over the catalyst is the crucial reason for the markedly improved photocatalytic performance and inhibition of NO₂ production. Among them, Bi@BiOBr/C-2 has the most positive DeNOx index (+0.68) owing to the suitable content of Bi-metal and OVs. These results were well indicative of the prominent photocatalytic performance and stability of the as-synthesized samples.

3.4. Optical and electrochemical properties

The UV-vis diffuse reflectance spectroscopy (UV-vis DRS) optical absorption of the acquired specimens was delivered in Fig. 4a. It can be observed that Bi-MOF has considerable absorption exclusively on the ultraviolet side of the spectrum, and its corresponding absorption edge is around 350 nm. In contrast, BiOBr/C samples exhibit additional partial absorption in the visible range, with the absorption edge extending to 430 nm. Additionally, with the increase of Bi-metal content, the absorption spectrum of the Bi@BiOBr/C emerges a redshift and reflects a significant light absorption in the 400–800 nm range. These results are attributed to (i) generally, the Bi-metal with SPR effect can capture various frequencies of light and enhance the response of visible light owing to its internal free electrons [48]; (ii) the Bi-metal is also able to be employed as an electron donor to change the transport pathway and shorten the migration distance of carriers, thus effectively enhancing the

separation efficiency of carriers [49]; (iii) the electronic states induced by OVs in the bandgap are capable to trigger the visible light response of photocatalysts [50,51]. Our artful synthetic methods realized the simultaneous introduction of Bi-metal and OVs to Bi@BiOBr/C, which successfully boosts the visible light response and the reactivity of photocatalysts.

On the other hand, it is well-known that the low recombination rate of photo-excited electrons and holes is favorable for catalytic oxidation processes. Therefore, to comprehend the separation efficiency of photo-generated carriers in our systems, the photoluminescence spectra (PL), transient photocurrent spectroscopy (TPS), and electrochemical impedance spectra (EIS) measurements were executed. As shown in Fig. 4b, the fluorescence intensity of Bi@BiOBr/C samples is significantly lower than that of Bi-MOF and BiOBr/C, and the Bi@BiOBr/C-2 among them particularly exhibits the lowest PL intensity, confirming that the synergistic effect of Bi-metal and OVs greatly inhibits charge recombination, whereas the surplus Bi-metals would become the recombination centers unfortunately, as discussed in Section 3.3. The enhanced photo-carrier separation efficiency can be further verified by the photocurrent response curves. As revealed in Fig. 4c, the stronger photocurrent response of Bi@BiOBr/C-2 than Bi-MOF and BiOBr/C suggests its highest photo-carriers exploitation capability. Moreover, EIS analyses (Fig. 4d) show that the Bi@BiOBr/C-2 owns the comparatively smallest interfacial charge transfer resistance (R_{ct}), which promotes the transfer of electrons. The studies by PL, TPS, and EIS show that consistent with the trend of NO photocatalytic activity as shown in Fig. 3a, the Bi@BiOBr/C-2 photocatalyst possesses the fastest carrier transport efficiency and the lowest photo-excited carrier recombination rate compared with the precursors Bi-MOF and BiOBr/C, thereby endowing

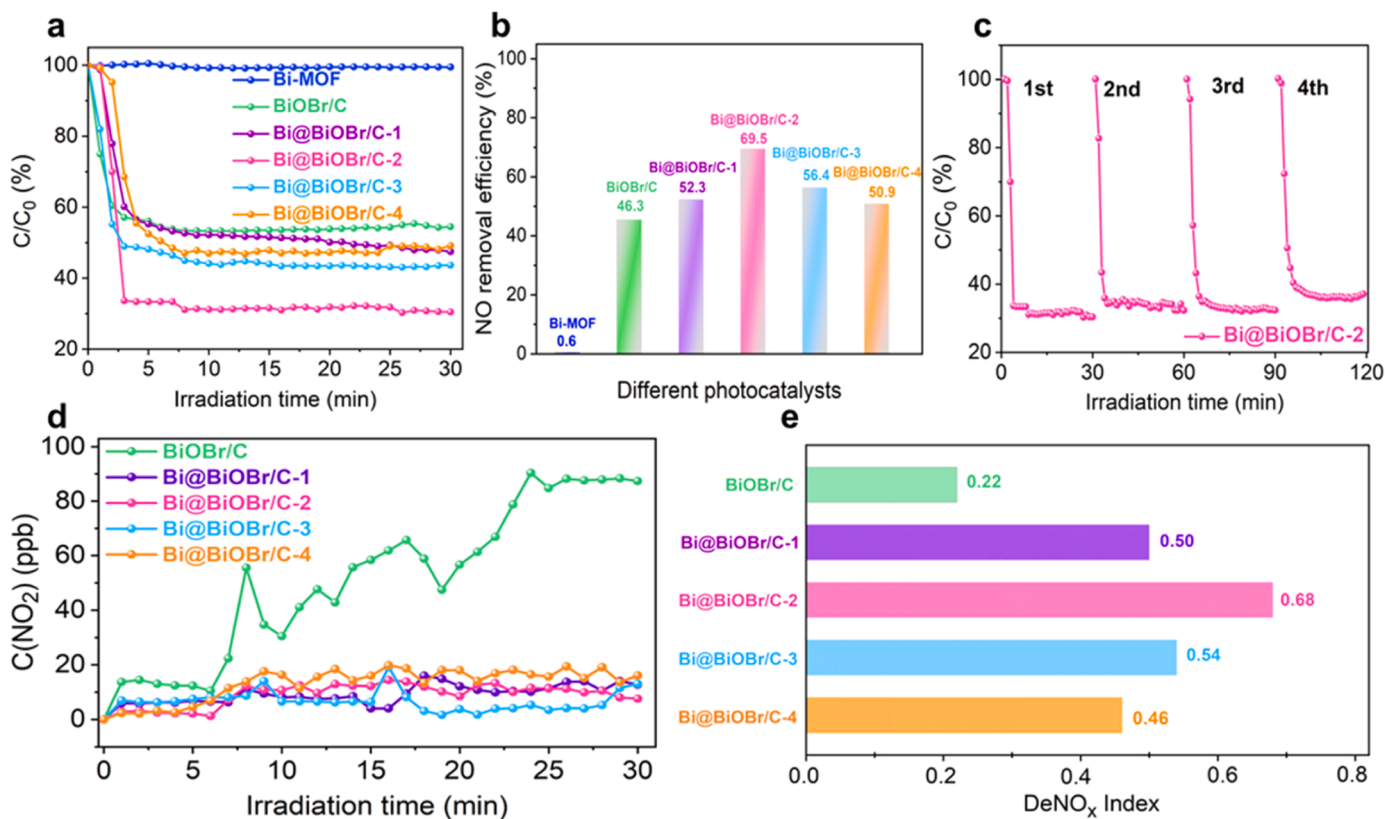


Fig. 3. Photocatalytic performances of the samples Bi-MOF, BiOBr/C, and Bi@BiOBr/C-X for NO removal (a)-(b), four cyclic tests using the same Bi@BiOBr/C-2 sample (c), the amount of NO_2 generated (d), and the DeNO_x index values for serial specimens (e).

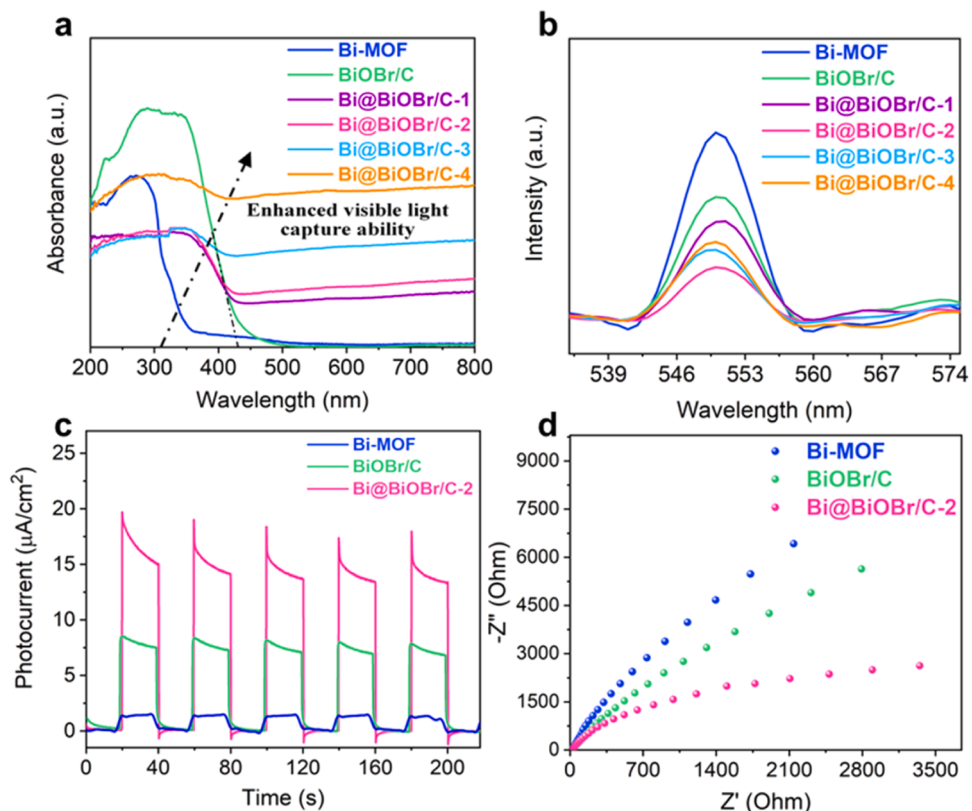


Fig. 4. UV-vis diffuse reflectance pattern (a) and the photoluminescence spectrum (b) of the fresh specimens, and photocurrents (c) and the Nyquist diagrams (d) examinations of Bi-MOF, BiOBr/C as well Bi@BiOBr/C-2.

Bi@BiOBr/C-2 with better photocatalytic behavior.

3.5. Photocatalytic reaction mechanism for NO oxidation

To acquire a comprehension of the influence of active radicals generated during the photocatalytic NO oxidation process, a series of free radical trapping experiments were performed over the Bi@BiOBr/C-2 sample. Tert-butyl alcohol (TBA), potassium dichromate ($K_2Cr_2O_7$), p-benzoquinone (PBQ), and potassium iodide (KI) were selected as scavengers to eliminate hydroxyl radicals ($\bullet OH$), electrons (e^-), superoxide radicals ($\bullet O_2^-$), and holes (h^+) during the reactions, respectively. As shown in Fig. 5(a), the addition of PBQ and $K_2Cr_2O_7$ into Bi@BiOBr/C-2 significantly suppresses the photocatalytic reactivity and practically no NO is eliminated under 30 min of light irradiation, implying that $\bullet O_2^-$ and e^- are crucial contributors to the NO abatement. Additionally, h^+ also contributes significantly to the photocatalytic NO oxidation process. It should be noted that $\bullet OH$ is not involved in the NO oxidation process since the photocatalytic performance is not significantly hindered upon adding the scavenger (TBA) of $\bullet OH$.

After distinguishing the roles of active radicals during the reactions, we then monitored their production in the Bi@BiOBr/C-2 system by electron spin resonance (ESR) measurements. As shown in Fig. 5(b), the ESR profile of BiOBr/C and Bi@BiOBr/C-2 exhibit no apparent signal peaks for $\bullet O_2^-$ under dark conditions, which were just monitored after 5 mins visible light irradiation and further boosted after 15 mins illumination. Furthermore, the ESR signal of DMPO- $\bullet O_2^-$ of Bi@BiOBr/C-2 is significantly enhanced compared with BiOBr/C, consistent with the photocatalytic performance (Fig. 3a). However, the ESR signal of Bi@BiOBr/C-2 demonstrates no obvious signal peaks for DMPO- $\bullet OH$ under both dark and illumination settings (Fig. 5c). Through the capture experiments and ESR assessments, it was ascertained that $\bullet O_2^-$ and h^+ are crucial reactive species to the photocatalytic abatement of NO.

To investigate how to effectively eliminate the NO, in situ DRIFTS real-time monitoring was performed to assess the intermediate/final substances absorbed on the BiOBr/C and Bi@BiOBr/C-2. The assignment of IR peaks during NO adsorption and oxidation is presented in Table 1. The time-dependent characteristic peaks of NO and intermediates during dark adsorption on the BiOBr/C and Bi@BiOBr/C-2 surfaces are shown in Fig. 6a and b. When the BiOBr/C and Bi@BiOBr/C-2 photocatalyst was placed in the mixed gases of O_2 and NO, multitudinous bands were monitored, and the intensity progressively enhanced with the elongation of time. During the dark adsorption process of BiOBr/C, the weak adsorption peaks at 1121 and 1633 cm^{-1} are allocated to the nitrites (NO_2^-) species, while the adsorption peaks at 1350 cm^{-1} are allocated to the nitrates (NO_3^-) species (Fig. 6a). Note-worthy is the fact that the adsorption peaks of NO_2^- and NO_3^- were also

Table 1

IR band distributions for NO adsorption and photoreaction processes over BiOBr/C and Bi@BiOBr/C-2.

Band positions (cm^{-1})	Surface species	References
1003	NO_3^- (bridged)	[52]
1117, 1263, 1472	NO_2^- (monodentate)	[53]
1343	NO_3^- (monodentate)	[54]
1716	NO^+	[55]
2335, 2400	NO_3^- (bidentate)	[56]
2906, 2948	NO_3^- (bridged)	[57]

detected in the dark adsorption stage of the Bi@BiOBr/C-2 photocatalyst, and the adsorption peaks at 1068 and 1594 cm^{-1} are allocated to the nitrites (NO_2^-) species, while the adsorption peaks at 1343 and 2359 cm^{-1} are attributed to the nitrates (NO_3^-) species (Fig. 6b). The Bi@BiOBr/C-2 photocatalyst produces more bands, which is mainly attributed to the possible activation of the adsorbed oxygen by photo-electrons captured by Bi-metal and OVs in Bi@BiOBr/C-2 photocatalyst, leading to the direct generation of NO_2^- and NO_3^- without light irradiation. After the mixed gas in the catalytic system reached the adsorption equilibrium on the surface of the BiOBr/C and Bi@BiOBr/C-2 sample, the time-dependent infrared spectra of the catalyst were recorded under visible light irradiation. In the process of illumination, the adsorption peaks of 1117, 1263, and 1472 cm^{-1} on the BiOBr/C surface are attributed to species NO_2^- , while the peak of 2335 and 2948 cm^{-1} are attributed to species NO_3^- (Fig. 6c). Compared with BiOBr/C, the adsorption peak of NO_3^- species gradually increases with the prolongation of the irradiation time (from 1 min to 30 min), demonstrating that the adsorbed NO is converted into the final products by the photocatalytic reaction on the surface of Bi@BiOBr/C-2 photocatalyst (Fig. 6d). Through further observation, the evident absorption peaks about NO_3^- species (at 1003, 2400, 2906, and 2948 cm^{-1}), NO_2^- species (at 1483 cm^{-1}), and a special intermediate species NO^+ (at 1716 cm^{-1}) can be monitored over Bi@BiOBr/C-2. The distribution of intermediates was significantly reduced, consistent with the formation of toxic intermediates (Fig. 3d), indicating that Bi@BiOBr/C-2 photocatalyst can selectively convert NO. Additionally, it can be seen that the peak intensity of the Bi@BiOBr/C-2 is substantially stronger than that of the Bi@BiOBr/C-2-Ads, and the final substances (NO_3^-) on the surface of the Bi@BiOBr/C-2 increasing. This is mainly because a large amount of NO_3^- can be generated under the interaction of NO with $\bullet O_2^-$ or h^+ during the photoreaction process, while the generation of NO^+ can be allocated to the trap of positive charges from OVs by nitrite. Then NO^+ is oxidized by $\bullet O_2^-$ or h^+ to form NO_3^- species, indicating that the presence of OVs in Bi@BiOBr/C-2 can promote the activation of NO and improve the photocatalytic abatement of NO by forming NO^+ . Hence, following the

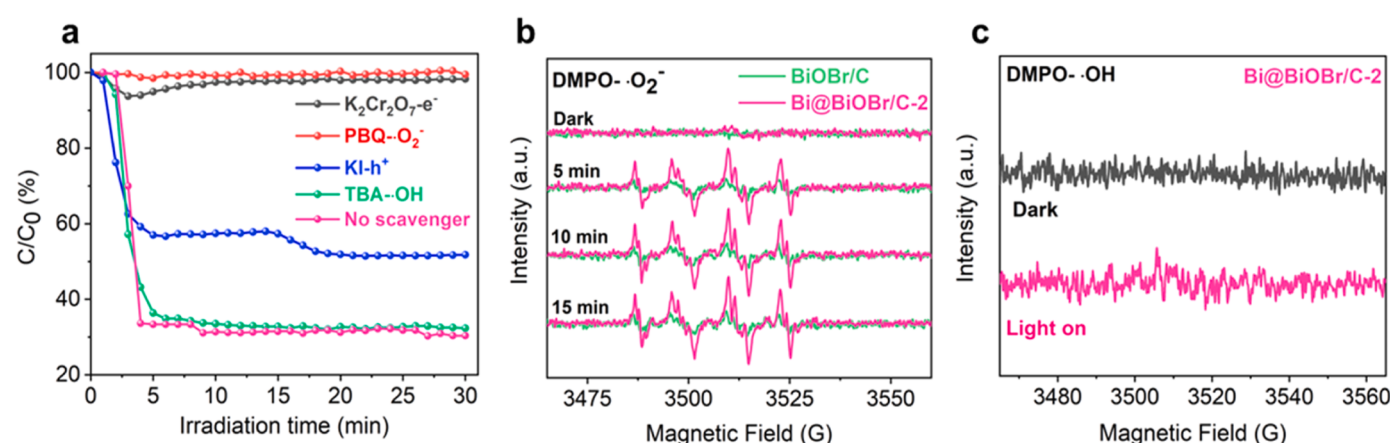


Fig. 5. The effects of various scavengers on NO abatement on Bi@BiOBr/C-2 (a), DMPO ESR spectrum of $\bullet O_2^-$ in dimethyl sulfoxide dispersions in the dark and under visible light irradiation (b), DMPO ESR spectrum of $\bullet OH$ in water dispersions(c).

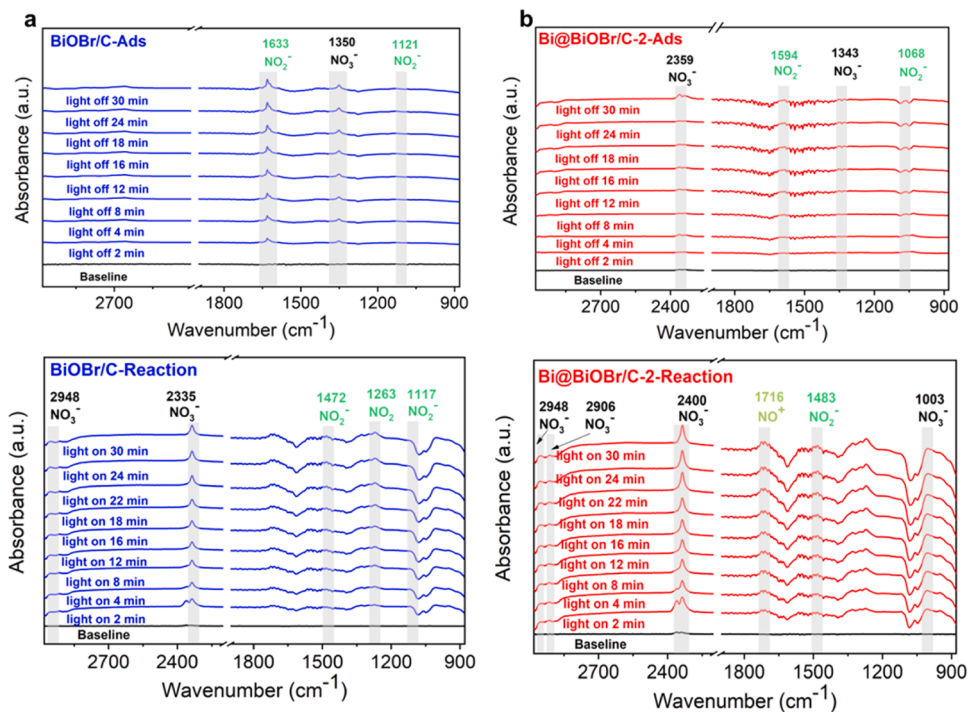


Fig. 6. In situ FT-IR spectrum of NO adsorption (a and b) and photoreaction (c and d) procedures on BiOBr/C and Bi@BiOBr/C-2.

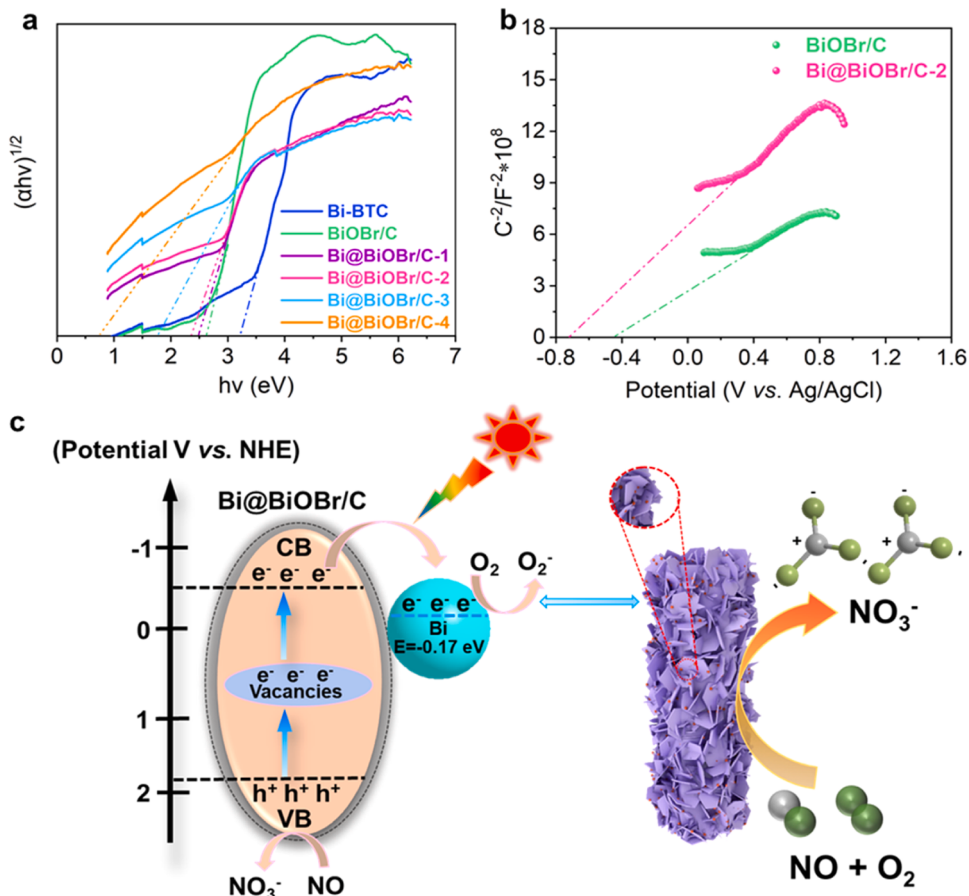
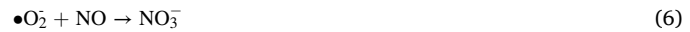


Fig. 7. Energy band gaps (E_g) of photocatalysts (a), Mott-Schottky plots of Bi@BiOBr/C-2 sample (b), the detailed photocatalytic NO removal mechanism of Bi-metal and OVs co-modified Bi@BiOBr/C-2 (c).

findings of the ESR investigation, Bi@BiOBr/C-2 can generate more $\bullet\text{O}_2^-$ active species to boost the photocatalytic oxidation of NO.

To further understand the free radical transfer pathway during NO photocatalytic oxidation in detail, it is necessary to investigate the relative band edges of semiconductors. The band gap energy of the specimens was determined according to the Kubelka-Munk formula: $a\hbar\nu = A(\hbar\nu - E_g)^{1/2}$, where a , \hbar , ν , A , and E_g represent the absorption coefficient, the Planck constant, optical frequency, constant, and the bandgap energy, respectively. The approximative bandgap energy of Bi@BiOBr/C-2 is 2.36 eV (Fig. 7a). Furthermore, Bi@BiOBr/C-2 is a class of n-type semiconductors, as shown in the Mott-Schottky plots (Fig. 7b). The flat band potential of Bi@BiOBr-2 can be obtained from the intercept of the epitaxial straight line ($Y = 0$), determined to be -0.72 eV versus Ag/AgCl. Moreover, the flat band potential is supposed to correspond to the Fermi level (E_F) of the photocatalysts, and the value of E_F is close to the CB of the n-type semiconductor. Therefore, the CB value of Bi@BiOBr/C-2 can be calculated to be -0.52 eV versus NHE. Based on this, combined with the E_g values acquired from the Tauc diagram, the energy band structure and free radical reaction process of the Bi@BiOBr/C-2 photocatalyst are shown in Fig. 7c. In photocatalytic removal of NO, BiOBr serves as a semiconductor photocatalyst. Under visible light irradiation, BiOBr absorbs photons and generates electron-hole pairs, and then the photogenerated electrons in its CB are transferred to Bi nanoparticles and participate in the addressed reaction. Meanwhile, the OVs in BiOBr can act as active centers, which play a crucial role in the electronic reconfiguration of the system, facilitating the adsorption/activation of small molecules (e.g., NO and O_2) and the formation of reactive species ($\bullet\text{O}_2^-$). As for graphitic carbon, it serves as an electron mediator and an electron-migration bridge between BiOBr and Bi nanoparticles (BiOBr \rightarrow graphitic carbon \rightarrow Bi nanoparticles), enhancing the separation and utilization of charge carriers and improving the photocatalytic performance. Additionally, in regard to Bi nanoparticles, they act as the active sites for the oxidation of NO to NO_3^- . When exposed to visible light, Bi nanoparticles collect photoelectrons from the CB of BiOBr and react with O_2 to generate strong oxides species ($\bullet\text{O}_2^-$), thus facilitating NO removal. Together, these factors work synergistically to catalyze the conversion of NO in the addressed reaction. Furthermore, the detailed reaction mechanism of free radicals during

the photocatalytic NO oxidation pathway is illustrated in Eqs. (1)–(7). After illumination, the Bi@BiOBr/C-2 photocatalyst produces $e^- - h^+$ pairs, and O_2 is reduced by e^- to form active radical $\bullet\text{O}_2^-$, which oxidizes NO to NO_3^- product. Additionally, h^+ also serves a crucial function in the ultimate conversion of NO into NO_3^- in the ambient atmosphere.



We employed DFT calculations to understand the charge transfer mechanism in Bi@BiOBr/C-2 systems. Generally, the main factor retarding the photo-carriers transfer from the semiconductor to the metal is the Schottky barrier formed in the vicinity of the interface [58], which has been eliminated and a preferable Ohmic contact was built in our Bi@BiOBr/C-2 system by the graphitic carbon between BiOBr and Bi nanoparticles. As shown in Fig. 8a, we chose the graphene to model the graphitic carbon on the stoichiometric BiOBr, and the work functions (WF) of graphitic carbon and BiOBr were estimated to 4.08 eV and 6.92 eV respectively according to the formula $WF = E_{\text{Vac}} - EF$ (E_{Vac} : Vacuum energy level, EF : Fermi energy level), which indicated that an electron-migration from graphitic C to BiOBr would happen when they contact each other (forming a heterojunction, Fig. 8b). Further DOS analyses also demonstrated the EF of BiOBr and graphitic carbon would rise and fall severally until the EF equilibrium is reached (Fig. 8c). As a consequence, an IEF near the interface would generate and result in a downward band bending for BiOBr (Ohmic contact in Bi@BiOBr/C-2 system, Fig. 8d), different from the Schottky junction (upward band bending, usually formed in Bi@BiOBr [59]). This particular Ohmic contact facilitates the photoelectrons in BiOBr to transfer to graphitic carbon without any energy barrier, promoting the photo-carrier

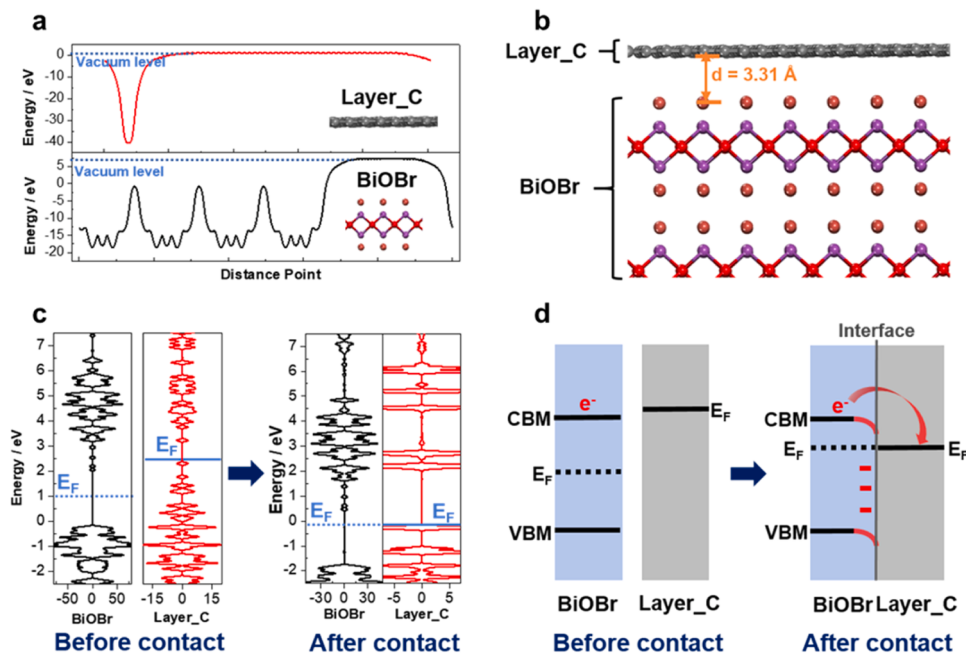


Fig. 8. The calculated local potential (Z direction) diagrams and atomic structures (insets) of graphitic C (upper) and BiOBr (under) (a), the calculated heterojunction structure of graphitic C and BiOBr, in which the optimized distance between the two materials is shown (b), the changes of electronic density of states (DOS) before and after BiOBr and graphitic C contact (c), the schematic diagram of the band structures of BiOBr and graphitic C before and after contact (d).

separation in BiOBr and creating an efficient electron transfer pathway in our Bi@BiOBr/C-2 system, i.e., “BiOBr → graphitic carbon → Bi nanoparticles”. Such results were further supported by the DOS analyses for the oxygen-deficient BiOBr (Fig. S7), which is closer to the real situation (Fig. 1c). The exceptional tunability of the Ohmic contact for interfacial charge transfer was also reported by Liu et al. in 2023, who altered the IEF direction of Bi/Bi₂MoO₆ by modifying Bi₂MoO₆ with oxygen vacancies, resulting in favorable charge transfer efficiency [60]. Therefore, our results demonstrated that the construction of an Ohmic contact strategy with graphite carbon loading in the Bi@BiOBr/C-2 photocatalyst system is an important factor in improving the charge transfer efficiency.

4. Conclusion

In summary, we have effectively integrated a Bi-metal and OV co-modified BiOBr/C (Bi@BiOBr/C) by using a facile halogenation treatment and subsequent chemical reduction method. The comprehensive results indicate that the optimized Bi@BiOBr /C-2 has the highest photocatalytic removal efficiency of 69.5 % for ppb-level atmospheric NO and inhibits the generation of toxic intermediate NO₂. The enhanced photocatalytic performance is owing to precisely constructed electron transport channels with loaded graphitic carbon as a bridge (i.e., BiOBr → graphitic carbon → Bi nanoparticles), which not only promotes the photo-carrier separation in BiOBr but also downshifts the photo-carrier recombination by tailoring the electron migration directional. Further DFT calculations demonstrated the built-in graphitic carbon reconstructs an Ohmic contact with BiOBr and eliminates the Schottky barrier between BiOBr and Bi nanoparticles, hiking the photoelectron transfer efficiency. Moreover, the synergistic effect of plasmonic Bi and OVs over Bi@BiOBr/C boosts the adsorption and photocatalytic removal of NO. All of them are pivotal factors to generating sufficient active superoxide radicals in the catalytic process to effectively realize NO conversion. Therefore, we believe that this study can provide a novel strategy for efficient photo-oxidation of gaseous pollutants by reasonably constructing atomic-level interface channels and realizing directional electron transfer.

CRediT authorship contribution statement

Ximing Li: Experimental, Methodology, Data curation, Validation, Writing–original draft. **Qibing Dong:** Formal analysis, Writing - review & editing. **Fei Li:** Formal analysis, Software, Supervision, Writing - review & editing. **Qiuhibi Zhu:** Validation, Visualization. **Qingyun Tian:** Writing – review & editing. **Lin Tian:** Investigation. **Yiyin Zhu:** Validation, Visualization. **Bao Pan:** Writing - review & editing. **Mohsen Padervand:** Supervision, Writing-reviewing and editing. **Chuanyi Wang:** Supervision, Writing-review and editing, Project administration, Funding acquisition.

Declaration of Competing Interest

The authors declare that they have no known competing financial interests or personal relationships that could have appeared to influence the work reported in this paper.

Data Availability

The authors do not have permission to share data.

Acknowledgements

This work was supported by the National Natural Science Foundation of China (52161145409, 21976116), SAEFA of China (“Belt and Road” Innovative Talent Exchange Foreign Expert Project # 2021041001L) (High-end Foreign Expert Project), Iran National Science Foundation

(INSF) (4001153), and Alexander-von-Humboldt Foundation of Germany (Group-Linkage Program).

Appendix A. Supporting information

Supplementary data associated with this article can be found in the online version at doi:10.1016/j.apcatb.2023.123238.

References

- [1] J.K. Gao, Q. Huang, Y.H. Wu, Y.Q. Lan, B.L. Chen, Metal–Organic frameworks for photo/electrocatalysis, *Adv. Energy Sustain. Res.* 12 (2021) 2100033–2100094.
- [2] R.T. Guo, W.G. Pan, X.B. Zhang, J.X. Ren, Q. Jin, H.J. Xu, J. Wu, Removal of NO by using Fenton reagent solution in a lab-scale bubbling reactor, *Fuel* 90 (2011) 3295–3298.
- [3] J.A. Rodriguez, T. Jirsak, G. Liu, J. Hrbek, J. Dvorak, A. Maiti, Chemistry of NO₂ on oxide surfaces: formation of NO₃ on TiO₂(110) and NO₂↔O vacancy interactions, *J. Am. Chem. Soc.* 123 (2001) 9597–9605.
- [4] S. Medinets, U. Skiba, H. Rennenberg, K. Butterbach-Bahl, A review of soil NO transformation: associated processes and possible physiological significance on organisms, *Soil Biol. Biochem.* 80 (2015) 92–117.
- [5] L. Yang, P. Wang, J. Yin, C. Wang, G. Dong, Y. Wang, W. Ho, Engineering of reduced graphene oxide on nanosheet-g-C₃N₄/perylene imide heterojunction for enhanced photocatalytic redox performance, *Appl. Catal. B* 250 (2019) 42–51.
- [6] G. Liu, Y. Huang, H. Lv, H. Wang, Y. Zeng, M. Yuan, Q. Meng, C. Wang, Confining single-atom Pd on g-C₃N₄ with carbon vacancies towards enhanced photocatalytic NO conversion, *Appl. Catal. B: Environ.* 284 (2021), 119683.
- [7] L. Zhao, G. Dong, L. Zhang, Y. Lu, Y. Huang, Photocatalytic nitrogen oxide removal activity improved step-by-step through serial multistep Cu modifications, *ACS Appl. Mater. Interfaces* 11 (2019) 10042–10051.
- [8] G. Dong, L. Yang, F. Wang, L. Zang, C. Wang, Removal of nitric oxide through visible light photocatalysis by g-C₃N₄ modified with perylene imides, *ACS Catal.* 6 (2016) 6511–6519.
- [9] P. Granger, V.I. Parvulescu, Catalytic NO_x abatement systems for mobile sources: from three-way to lean burn after-treatment technologies, *Chem. Rev.* 111 (2011) 3155–3207.
- [10] K. Erme, I. Jogi, Metal oxides as catalysts and adsorbents in ozone oxidation of NO_x, *Environ. Sci. Technol.* 53 (2019) 5266–5271.
- [11] B. Xiao, P.S. Wheatley, X. Zhao, A.J. Fletcher, S. Fox, A.G. Rossi, I.L. Megson, S. Bordiga, L. Regli, K.M. Thomas, R.E. Morris, High-capacity hydrogen and nitric oxide adsorption and storage in a metal–organic framework, *J. Am. Chem. Soc.* 129 (2007) 1203–1209.
- [12] P. Zhu, X. Yin, X. Gao, G. Dong, J. Xu, C. Wang, Enhanced photocatalytic NO removal and toxic NO₂ production inhibition over ZIF-8-derived ZnO nanoparticles with controllable amount of oxygen vacancies, *Chin. J. Catal.* 42 (2021) 175–183.
- [13] W.J. Ong, L.L. Tan, Y.H. Ng, S.T. Yong, S.P. Chai, Graphitic carbon nitride (g-C₃N₄)-based photocatalysts for artificial photosynthesis and environmental remediation: are we a step closer to achieving sustainability? *Chem. Rev.* 116 (2016) 7159–7329.
- [14] Q. Zhang, Y. Huang, S. Peng, Y. Zhang, Z. Shen, J.J. Cao, W. Ho, S.C. Lee, D.Y. H. Pui, Perovskite LaFeO₃-SrTiO₃ composite for synergistically enhanced NO removal under visible light excitation, *Appl. Catal. B Environ.* 204 (2017) 346–357.
- [15] B. Pan, Y. Wu, B. Rhimi, J. Qin, Y. Huang, M. Yuan, C. Wang, Oxygen-doping of ZnIn₂S₄ nanosheets towards boosted photocatalytic CO₂ reduction, *J. Energy Chem.* 57 (2021) 1–9.
- [16] M. Takeuchi, H. Yamashita, M. Matsuoka, M. Anpo, T. Hirao, N. Itoh, N. Iwamoto, Photocatalytic decomposition of NO under visible light irradiation on the Cr-ion-implanted TiO₂ thin film photocatalyst, *Catal. Lett.* 67 (2000) 135–137.
- [17] Z. Liu, L. Ma, A.S.M. Junaid, NO and NO₂ adsorption on Al₂O₃ and Ga modified Al₂O₃ surfaces: a density functional theory study, *J. Phys. Chem. C* 114 (2010) 4445–4450.
- [18] S.R. Zhu, M.K. Wu, W.N. Zhao, P.F. Liu, F.Y. Yi, G.C. Li, K. Tao, L. Han, In situ growth of metal–organic framework on BiOBr 2D material with excellent photocatalytic activity for dye degradation, *Cryst. Growth Des.* 17 (2017) 2309–2313.
- [19] H. Li, J. Liu, X. Liang, W. Hou, X. Tao, Enhanced visible light photocatalytic activity of bismuth oxybromide lamellas with decreasing lamella thicknesses, *J. Mater. Chem. A* 2 (2014) 8926–8932.
- [20] X. Zheng, L. Feng, Y. Dou, H. Guo, Y. Liang, G. Li, J. He, P. Liu, J. He, High carrier separation efficiency in morphology-controlled BiOBr/C Schottky junctions for photocatalytic overall water splitting, *ACS Nano* 15 (2021) 13209–13219.
- [21] H. Zhang, Y. Yang, Z. Zhou, Y. Zhao, L. Liu, Enhanced photocatalytic properties in biobr nanosheets with dominantly exposed (102) facets, *J. Phys. Chem. C* 118 (2014) 14662–14669.
- [22] X. Shi, P. Wang, W. Li, Y. Bai, H. Xie, Y. Zhou, L. Ye, Change in photocatalytic NO removal mechanisms of ultrathin BiOBr/BiOI via NO₃ adsorption, *Appl. Catal. B Environ.* 243 (2019) 322–329.
- [23] M. Shi, G. Li, J. Li, X. Jin, X. Tao, B. Zeng, E.A. Pidko, R. Li, C. Li, Intrinsic facet-dependent reactivity of well-defined BiOBr nanosheets on, in: *Angew Photocatalytic Water Splitting* (Ed.), *Chem.*, Int., 59, 2020, pp. 6590–6595.

- [24] Y. Liu, Y. Yin, X. Jia, X. Cui, C. Tian, Y. Sang, H. Liu, Synthesis process and photocatalytic properties of BiOBr nanosheets for gaseous benzene, *Environ. Sci. Pollut. Res.* 23 (2016) 17525–17531.
- [25] P. Li, Z. Zhou, Q. Wang, M. Guo, S. Chen, J. Low, R. Long, W. Liu, P. Ding, Y. Wu, Y. Xiong, Visible-light-driven nitrogen fixation catalyzed by $\text{Bi}_5\text{O}_7\text{Br}$ nanostructures: enhanced performance by oxygen vacancies, *J. Am. Chem. Soc.* 142 (2020) 12430–12439.
- [26] Z. Li, G. Huang, K. Liu, X. Tang, Q. Peng, J. Huang, M. Ao, G. Zhang, Hierarchical BiOX (X=Cl, Br, I) microrods derived from Bismuth-MOFs: In situ synthesis, photocatalytic activity and mechanism, *J. Clean. Prod.* 272 (2020) 122892–122902.
- [27] Y.S. Kang, Y. Lu, K. Chen, Y. Zhao, P. Wang, W.Y. Sun, Metal-organic frameworks with catalytic centers: From synthesis to catalytic application, *Coord. Chem. Rev.* 378 (2019) 262–280.
- [28] L.Y. Chen, Q. Xu, Metal-organic framework composites for catalysis, *Matter* 1 (2019) 57–89.
- [29] M.Z. Hussain, Z. Yang, Z. Huang, Q. Jia, Y. Zhu, Y. Xia, Recent advances in metal-organic frameworks derived nanocomposites for photocatalytic applications in energy and environment, *Adv. Sci.* 8 (2021) 2100625–2100654.
- [30] S. Xiao, D. Pan, R. Liang, W. Dai, Q. Zhang, G. Zhang, C. Su, H. Li, W. Chen, Bimetal MOF derived mesocrystal ZnCo_2O_4 on rGO with high performance in visible-light photocatalytic NO oxidation, *Appl. Catal., B* 236 (2018) 304–313.
- [31] D. Liu, D. Chen, N. Li, Q. Xu, H. Li, J. He, J. Lu, ZIF-67-derived 3D hollow mesoporous crystalline Co_3O_4 wrapped by 2D g-C₃N₄ nanosheets for photocatalytic removal of nitric oxide, *Small* 15 (2019) 1902291–1902301.
- [32] X. Li, W. Zhang, J. Li, G. Jiang, Y. Zhou, S. Lee, F. Dong, Transformation pathway and toxic intermediates inhibition of photocatalytic NO removal on designed Bi metal@defective $\text{Bi}_2\text{O}_2\text{SiO}_3$, *Appl. Catal. B* 241 (2019) 187–195.
- [33] P. Chen, H. Liu, Y. Sun, J. Li, W. Cui, L.A. Wang, W. Zhang, X. Yuan, Z. Wang, Y. Zhang, F. Dong, Bi metal prevents the deactivation of oxygen vacancies in $\text{Bi}_2\text{O}_2\text{CO}_3$ for stable and efficient photocatalytic NO abatement, *Appl. Catal. B Environ.* 264 (2020), 118545.
- [34] M. Sun, W. Zhang, Y. Sun, Y. Zhang, F. Dong, Synergistic integration of metallic Bi and defects on BiOI: Enhanced photocatalytic NO removal and conversion pathway, *Chin. J. Catal.* 40 (2019) 826–836.
- [35] Y. Li, M. Wen, Y. Wang, G. Tian, C. Wang, J. Zhao, Plasmonic hot electrons from oxygen vacancies for infrared light-driven catalytic CO_2 reduction on $\text{Bi}_2\text{O}_{3-x}$, *Angew. Chem. Int. Ed.* 60 (2021) 910–916.
- [36] F. Dong, T. Xiong, Y. Sun, Z. Zhao, Y. Zhou, X. Feng, Z. Wu, A semimetal bismuth element as a direct plasmonic photocatalyst, *Chem. Commun.* 50 (2014) 10386–10389.
- [37] H. Ouyang, N. Chen, G. Chang, X. Zhao, Y. Sun, S. Chen, H. Zhang, D. Yang, Selective capture of toxic selenite anions by bismuth-based metal-organic frameworks, *Angew. Chem., Int. Ed.* 57 (2018) 13197–13201.
- [38] G. Kresse, J. Furthmüller, Efficiency of ab-initio total energy calculations for metals and semiconductors using a plane-wave basis set, *Comp. Mater. Sci.* 6 (1996) 15–50.
- [39] G. Kresse, J. Furthmüller, Efficient iterative schemes for ab initio total-energy calculations using a plane-wave basis set, *Phys. Rev. B* 54 (1996) 11169–11186.
- [40] P.E. Blöchl, Projector augmented-wave method, *Phys. Rev. B* 50 (1994) 17953–17979.
- [41] G. Kresse, D. Joubert, From ultrasoft pseudopotentials to the projector augmented-wave method, *Phys. Rev. B* 59 (1999) 1758–1775.
- [42] J.P. Perdew, K. Burke, M. Ernzerhof, Generalized gradient approximation made simple, *Phys. Rev. Lett.* 77 (1996) 3865–3868.
- [43] M. Gu, Y. Li, M. Zhang, X. Zhang, Y. Shen, Y. Liu, F. Dong, Bismuth nanoparticles and oxygen vacancies synergistically attired Zn_2SnO_4 with optimized visible-light-active performance, *Nano Energy* 80 (2021), 105415.
- [44] Y. Tong, P. Chen, M. Zhang, T. Zhou, L. Zhang, W. Chu, C. Wu, Y. Xie, Oxygen vacancies confined in nickel molybdenum oxide porous nanosheets for promoted electrocatalytic urea oxidation, *ACS Catal.* 8 (2018) 1–7.
- [45] X. Ren, J. Li, X. Cao, B. Wang, Y. Zhang, Y. Wei, Synergistic effect of internal electric field and oxygen vacancy on the photocatalytic activity of BiOBr_{1-x} with isomorphous fluorine substitution, *J. Colloid Interface Sci.* 554 (2019) 500–511.
- [46] M. Gu, Y. Li, M. Zhang, X. Zhang, Y. Shen, Y. Liu, F. Dong, Bismuth nanoparticles and oxygen vacancies synergistically attired Zn_2SnO_4 with optimized visible-light-active performance, *Nano Energy* 80 (2021), 105415.
- [47] D. Zhang, H. Liu, C. Su, H. Li, Y. Geng, Combustion synthesis of highly efficient Bi/BiOBr visible light photocatalyst with synergistic effects of oxygen vacancies and surface plasma resonance, *Sep. Purif. Technol.* 218 (2019) 1–7.
- [48] Q. Zhu, R. Hailili, Y. Xin, Y. Zhou, Y. Huang, X. Pang, K. Zhang, P.K.J. Robertson, D.W. Bahnemann, C. Wang, Efficient full spectrum responsive photocatalytic NO conversion at $\text{Bi}_2\text{Ti}_2\text{O}_7$: Co-effect of plasmonic Bi and oxygen vacancies, *Appl. Catal. B Environ.* 319 (2022), 121888.
- [49] F. Dong, Z. Zhao, Y. Sun, Y. Zhang, S. Yan, Z. Wu, An advanced semimetal-organic Bi spheres-g-C₃N₄ nanohybrid with SPR-enhanced visible-light photocatalytic performance for NO purification, *Environ. Sci. Technol.* 49 (2015) 12432–12440.
- [50] W. Cui, L. Chen, J. Li, Y. Zhou, Y. Sun, G. Jiang, S.C. Lee, F. Dong, Ba-vacancy induces semiconductor-like photocatalysis on insulator BaSO_4 , *Appl. Catal. B Environ.* 253 (2019) 293–299.
- [51] F. Lei, Y. Sun, K. Liu, S. Gao, L. Liang, B. Pan, Y. Xie, Oxygen vacancies confined in ultrathin indium oxide porous sheets for promoted visible-light water splitting, *J. Am. Chem. Soc.* 136 (2014) 6826–6829.
- [52] Y.Y. Wang, K. Wang, J.L. Wang, X.Y. Wu, G.K. Zhang, Sb₂WO₆/BiOBr 2D nanocomposite S-scheme photocatalyst for NO removal, *J. Mater. Sci. Technol.* 56 (2020) 236–243.
- [53] H.Z. Wu, R.M. Chen, H. Wang, W. Cui, J.Y. Li, J.D. Wang, C.W. Yuan, L. Zhuo, Y. X. Zhang, F. Dong, An atomic insight into BiOBr/La₂Ti₂O₇ p-n heterojunctions: interfacial charge transfer pathway and photocatalysis mechanism, *Catal. Sci. Technol.* 10 (2020) 826–834.
- [54] M. Kantcheva, Identification, stability, and reactivity of NO_x species adsorbed on titania-supported manganese catalysts, *J. Catal.* 204 (2001) 479–494.
- [55] Y. Li, M. Gu, M. Zhang, X. Zhang, K. Lv, Y. Liu, W. Ho, F. Dong, C₃N₄ with engineered three coordinated (N₃C) nitrogen vacancy boosts the production of $^1\text{O}_2$ for Efficient and stable NO photo-oxidation, *Chem. Eng. J.* 389 (2020), 124421.
- [56] W.J. He, Y.J. Sun, G.M. Jiang, H.W. Huang, X.M. Zhang, F. Dong, Activation of amorphous Bi_2WO_6 with synchronous Bi metal and Bi_2O_3 coupling: Photocatalysis mechanism and reaction pathway, *Appl. Catal. B Environ.* 232 (2018) 340–347.
- [57] X.F. Tan, G.D. Qin, G. Cheng, X.J. Song, X. Chen, W.X. Dai, X.Z. Fu, Oxygen vacancies enhance photocatalytic removal of NO over an N-doped TiO_2 catalyst, *Catal. Sci. Technol.* 10 (2020) 6923–6934.
- [58] Y. Jiao, A. Hellman, Y. Fang, S. Gao, M. Käll, Schottky barrier formation and band bending revealed by first-principles calculations, *Sci. Rep.* 5 (2015) 11374.
- [59] X.A. Dong, W. Zhang, Y. Sun, J. Li, W. Cen, Z. Cui, H. Huang, F. Dong, Visible-light-induced charge transfer pathway and photocatalysis mechanism on Bi semimetal@ defective BiOBr hierarchical microspheres, *J. Catal.* 357 (2018) 41–50.
- [60] L. Liu, Z. Wang, J. Zhang, O. Ruzimuradov, K. Dai, J. Low, Tunable interfacial charge transfer in a 2D–2D composite for efficient visible-light-driven CO_2 conversion, *Adv. Mater.* (2023) 2300643.